NANO LETTERS

pubs.acs.org/NanoLett
Letter

Lithography-Defined Semiconductor Moirés with Anomalous In-Gap Quantum Hall States

Wei Pan,* D. Bruce Burckel, Catalin D. Spataru, Keshab R. Sapkota, Aaron J. Muhowski, Samuel D. Hawkins, John F. Klem, Layla S. Smith, Doyle A. Temple, Zachery A. Enderson, Zhigang Jiang, Komalavalli Thirunavukkuarasu, Li Xiang, Mykhaylo Ozerov, Dmitry Smirnov, Chang Niu, Peide D. Ye, Praveen Pai, and Fan Zhang*

Cite This: https://doi.org/10.1021/acs.nanolett.5c02180

ABSTRACT: Quantum materials and phenomena have attracted great interest for their potential applications in next-generation microelectronics and quantum-information technologies. In one especially interesting class of quantum materials, moiré superlattices (MSLs) formed by twisted bilayers of 2D materials, a wide range of novel phenomena are observed. However, there exist daunting challenges such as reproducibility and scalability of utilizing 2D MSLs for microelectronics and quantum technologies due to their exfoliate-tear-stack method. Here, we propose lithography-defined semiconductor MSLs, in which three fundamental parameters—electron−electron interaction, spin−orbit coupling, and band topology—are designable. We experimentally investigate quantum-transport properties in a moiré specimen made in an InAs quantum well. Strong anomalous in-gap states are observed within the same integer quantum Hall state. Our work opens up new horizons for studying 2D quantum-materials phenomena in semiconductors featuring superior industry-level quality and state-of-the-art technologies, and they may potentially enable new quantum-information and microelectronics technologies.

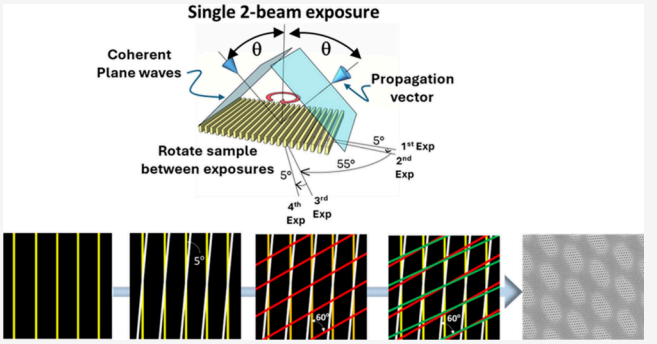

KEYWORDS: *lithography-defined moirés, compound semiconductor, flat bands, quantum Hall effect, in-gap states, artificial quantum materials*

Quantum materials are exciting classes of materials in which quantum phenomena emerge at macroscale without classical counterparts.[1] These materials and phenomena have attracted a great deal of interest for their potential applications in next-generation microelectronics and quantum-information technologies. In one especially interesting class, two of the same or similar atomically thin layers of 2D van der Waals (vdW) materials, such as graphene or transition-metal dichalcogenides (TMDs), are overlaid with a small twist angle or lattice mismatch, introducing a moiré periodicity as a new length scale and a moiré band structure as a new basis, not only for energy quantization but also for quantum geometry.[2−8] The so-formed moiré superlattices (MSLs) have become fertile ground for exploring quantum phenomena, such as the Hofstadter butterfly spectrum[9,10] and zero-magnetic-field fractional quantum anomalous Hall effect.[11−13] In particular, when twisted bilayer graphene is engineered at its "magic" twist angle, the low-energy moiré bands are nearly flat,[14,15] indicating that electrons are heavy and slow, with unusually strong electron−electron interactions. Indeed, a wide range of novel quantum phenomena have been observed, such as quantum geometric superconductivity[16−18] and orbital ferromagnetism.[19,20]

The established moiré quantum materials and phenomena are truly exciting. However, vdW MSLs are mainly fabricated using mechanical exfoliation followed by tear-and-stack methods. Thus, MSLs are not only challenging to reproduce because of the inevitable lattice relaxation and spatial inhomogeneity[3,21] but also incompatible with the state-of-the-art semiconductor processing technologies that exclusively address scalability. In this paper, we propose realizing lithography-defined MSLs[22] composed entirely of sophisticated bulk semiconductors (particularly III−V compound semiconductors such as InAs). In these semiconductor MSLs, our theoretical simulations show the formation of flat bands.

Received: April 15, 2025
Revised: June 3, 2025
Accepted: June 4, 2025

https://doi.org/10.1021/acs.nanolett.5c02180
Nano Lett. XXXX, XXX, XXX−XXX

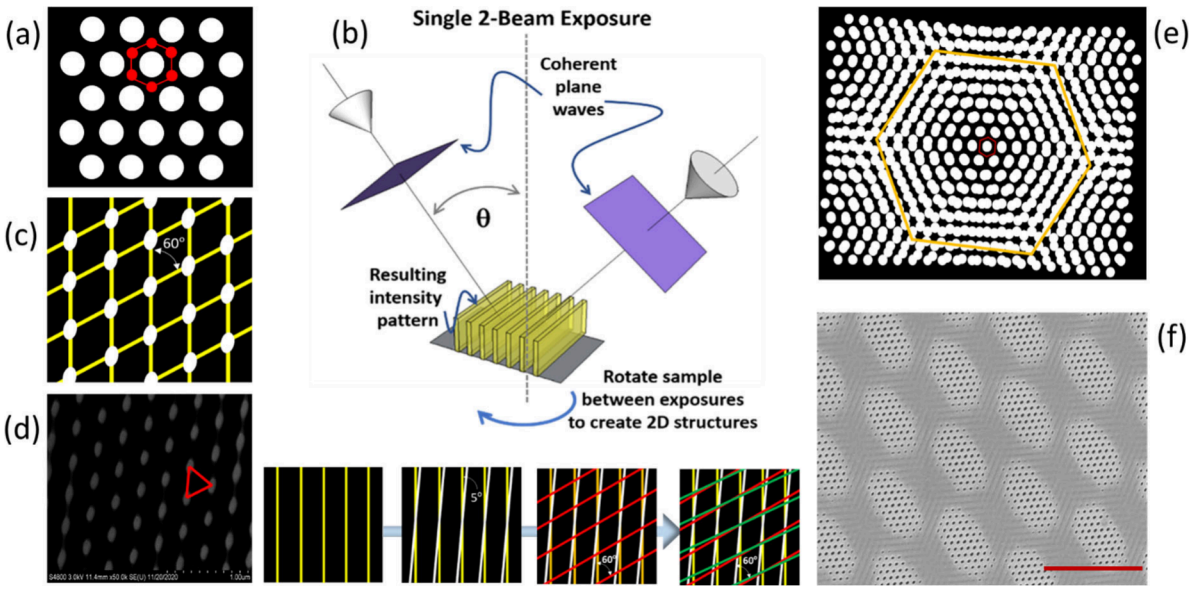

Figure 1. General scheme of creating MSLs in a 2DEG formed in a semiconductor QW. (a) Schematic representation of AG. The white dots represent holes etched through the 2DEG (black square), leaving the red areas forming a honeycomb lattice. (b) Schematic depiction of two-beam IL, where parallel lines of alternating intensity form due to the interference of two linearly polarized coherent plane waves. The bottom four panels show schematically how a lithography-defined MSL is fabricated using the IL method. (c) Schematic of two sets of parallel lines of a interference pattern with a twist angle of 60°. By adjusting the laser intensity and exposure time, only the photoresist at the crossing points (brown dots) is fully exposed. (d) SEM image of a triangular lattice of etched holes through a 2DEG in an InAs QW. (e) Schematic of two AG patterns with a twist angle of 5°. The large supercell is indicated by the yellow hexagon. (f) SEM image of a MSL in an InAs QW. The scale bar is 5 μm.

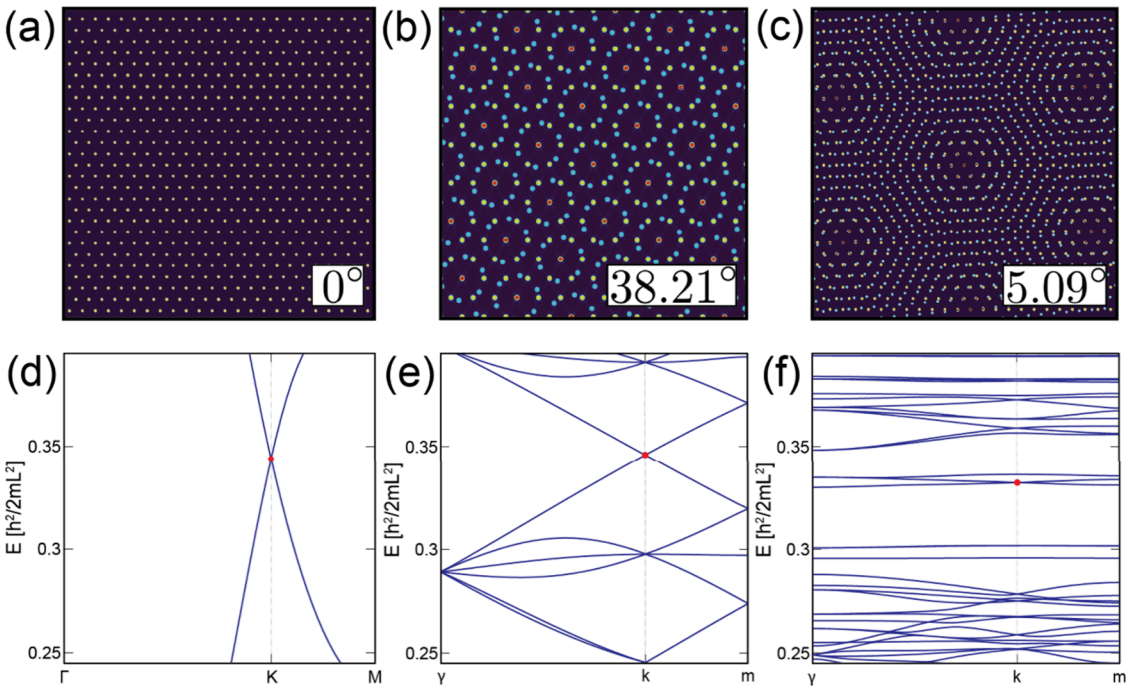

Figure 2. Plots of the real-space potential profiles and resulting band structures of the AG and MSL systems. For all potential holes, $V = 10\frac{h^2}{2mL^2}$ and $\frac{R}{L} = \frac{1}{9}$. (a) Plot of the muffin-tin potential profile that produces the AG. (b) Commensurate MSL pattern that appears by the rotation of a second set of the same AG by $\theta = 38.21°$. The yellow and blue potential holes indicate each of the two layers, and the red holes are where they overlap. (c) Same as part b but for a commensurate MSL pattern with $\theta = 5.09°$. (d–f) Calculated band structures of parts a–c, respectively. The red dots indicate the Dirac points.

Like in magic-angle twisted bilayer graphene or TMD moirés, these flat bands are expected to lead to heavy electrons with low kinetic energy and strong electron–electron interactions, giving rise to new strongly correlated electrons.

Figure 1 illustrates our general scheme of creating MSLs in a 2D electron gas (2DEG) formed in a quantum well (QW). As shown schematically in Figure 1a, we first pattern an in-plane triangular hole (white dots) array. Once the 2DEG in the hole

https://doi.org/10.1021/acs.nanolett.5c02180
Nano Lett. XXXX, XXX, XXX−XXX

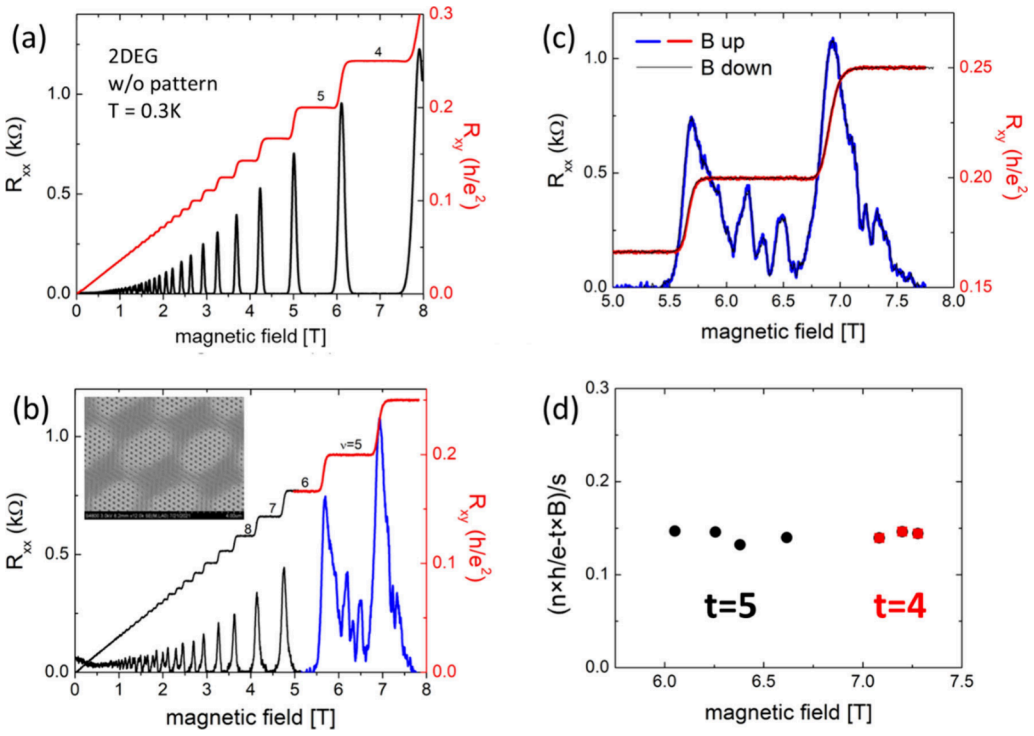

Figure 3. Anomalous in-gap states in lithography-defined semiconductor moiré. (a) Electronic transport coefficients, magnetoresistance R_{xx}, and Hall resistance R_{xy} of the 2DEG in an InAs QW. (b) R_{xx} and R_{xy} of a 2DEG-based moiré fabricated with the same QW as part a. The blue part highlights the anomalous in-gap states in the quantum Hall state at Landau level filling $\nu = 5$. The quantized Hal resistance is unaffected by these in-gap states. (c) R_{xx} (R_{xy}) traces for the magnetic field sweeping up and down. The two traces overlap perfectly, demonstrating the robustness of the in-gap states. (d) Diophantine analysis of the in-gap states. All of the data points show similar values of ∼0.15.

region is etched off, the unetched area forms a honeycomb lattice, namely, artificial graphene (AG),[23−25] as sketched by the red dots in Figure 1a. Note that the formation of the lateral AG superlattice creates Dirac minibands with a periodicity-dependent velocity that scales inversely with the superlattice constant.[23] Parts b−d of Figure 1 show the AG and MSLs device fabrication in an InAs QW in this work. Interferometric lithography (IL), which utilizes maskless exposure of a photoresist layer with two coherent UV-light beams (Figure 1b), is used to create the AG and MSLs. It provides a flexible, uniform, large-area nanolithographic capability. To pattern the AG, two separate exposures are used to create the triangular lattice in the resist prior to development. In detail, the interference pattern of two linearly polarized coherent plane waves is used to define the first set of parallel lines in commercially available negative tone photoresist (NR7-500P). Then the sample is rotated by 60° prior to development, and a second exposure is used to define the second set of lines. The exposure dose is controlled so that a triangular array of holes exists after postexposure bake and development (Figure 1c). The sample is then etched using reactive ion etching (RIE), and the resist is removed, yielding a triangular hole array in the 2DEG. Figure 1d shows a scanning electron microscopy (SEM) image of one such AG device.

Two identical AGs (AG1 and AG2) with an in-plane angular twist can also be patterned in the same 2DEG. An example of 5° is shown schematically in Figure 1e. As such, there emerges a much larger hexagonal lattice structure, i.e., a MSL indicated by the yellow hexagon. To create the MSL using IL, two separate, rotated AG patterns are created in the photoresist prior to development. By careful control of the angles between the four exposures for the AG patterns, the twist angle between AG1 and AG2 can be precisely defined without requiring any postprocessing alignment. The first set of parallel lines for AG1 is defined in the resist followed by the first set of parallel lines for AG2 with a twist angle of 5°. This is then followed by the second sets of lines for AG1 and AG2, respectively, at a twist angle of 60° with respective to each of the two first sets. The bottom four panels in Figure 1b show, schematically, the above process. The laser intensity and exposure time for each set of parallel lines are the same. After postexposure bake, photoresist development, and RIE, holes are etched through the 2DEG, and the designed MSL is produced. An SEM image of one such MSL device is shown in Figure 1f.

To verify the formation of flat bands in our artificial semiconductor MSL, now we show our band structure calculations in Figure 2. The effective-mass theory in conjunction with muffin-tin potentials is used to describe a 2DEG subjected to a periodic external potential (see Methods). We first show the results for an AG in Figure 2a,d. The strength of potential modulation is set to be 10 in units of $\frac{h^2}{2mL^2}$, where m is the effective mass of the 2DEG in a QW, L the lattice constant of the AG, and h the Planck constant. Consistent with a previous study,[23] mini Dirac cones merge in the superlattice band structure. Taking $m = 0.023m_e$ for InAs and $L = 200$ nm, the Dirac velocity is calculated to be $\sim 5.3 \times 10^4$ m/s; this is $\sim\frac{1}{20}$ of monolayer graphene's Fermi velocity, demonstrating that the energy bands become flatter with AG potential modulation. Figure 2 also includes two overlaid AG patterns with a commensurate twist angle of $\theta = 38.21°$ in Figure 2b and $\theta = 5.09°$ in Figure 2c. The strengths of potential modulation in AG1 (green color) and AG2 (light

https://doi.org/10.1021/acs.nanolett.5c02180
Nano Lett. XXXX, XXX, XXX−XXX

blue) are set to be $V_1 = V_2 = 10$ in units of $\frac{h^2}{2mL^2}$, and the lattice constants are identically L. Parts e and f of Figure 2 show the electronic band structures for these two commensurate MSLs, featuring mini Dirac points at nearly the same energy of the original Dirac point of AG1 in Figure 2b. At the large twist angle $\theta = 38.21°$, the Dirac velocity of the MSL is only reduced to ∼0.8 of that of AG, yet at the small twist angle $\theta = 5.09°$ close to the value of our experimental device, ultraflat bands (with Dirac velocity reduced to ∼0.1 of that of AG) separated from other minibands emerge. Note that the lattice constant can be made as small as $L = 20$ nm, which is within the capability of extreme-UV lithography. In the Supporting Information, we further show that the strength of Rashba spin−orbit coupling (SOC) in AG can be tuned by simply varying the lattice constant L. This may open a new avenue for AG spintronics.

Compared to vdW MSLs, semiconductor 2DEG-based MSLs add two powerful features: intrinsic spin−orbit coupling (SOC) and band gap/topology, and both are accurately designable and continuously tunable. This offers the unique advantage to controllably combine electron−electron interaction and SOC,[26] which may enable disentangling of those striking yet elusive quantum phenomena observed in their uncontrolled combinations in vdW MSLs. For example, superconductivity and correlated insulators with unconventional features have been observed in magic-angle TBG.[17] However, it is not yet clear whether and how spin and/or SOC play important roles in producing, enriching, and enhancing (or suppressing) them. To address this outstanding question, a TMD layer was intentionally added to the already delicate device.[27,28] However, it is challenging to control and determine the strength of the proximity-induced SOC. Another dimension of such superior design is band topology engineering of type II semiconductors such as InAs/GaSb by varying the well thicknesses[29] or applying an electric field,[30] in which Quantum spin Hall insulator[31] and excitonic insulator[32,33] have been achieved.

However, the lattice constant L of AG produced by the UV IL process is limited to ∼200 nm. For a 1° MSL, the MSL constant (L_m) is ∼10 μm and the carrier density hosted in the first miniband, $n_s = 8/(\sqrt{3}L_m^2)$,[17] is $\sim 10^6$ cm^{-2}. To raise n_s to a practical value, one can either increase the twist angle to ∼10° or lower L to the 20 nm range by employing e-beam lithography, focused-ion-beam milling,[34] or even EUV IL. This boosts n_s to $\sim 10^{11}$ cm^{-2} accessible to InAs QWs. Note that the magic angle of 2DEG-based MSL, if existent, should be much larger than that of twisted bilayer graphene because of a much smaller Dirac velocity and much stronger "interlayer" tunneling (as two AGs are defined in the same 2DEG).

In the following, we will present our experimental results of magnetotransport studies in a specimen of IL-fabricated 2DEG-based MSLs. Similar results have also been observed in other specimens cut from the same wafer. InAs QWs are chosen as the starting material for the following reason. It is known that the Fermi level of InAs normally pins above the bottom of the conduction band; this helps avoid the depletion length issue as encountered in GaAs QWs.[35] Figure 3a shows the longitudinal resistance R_{xx} and Hall resistance R_{xy} taken in a nonpatterned 2DEG in an InAs QW. At low B fields, R_{xx} displays the SdH oscillations, and R_{xy} is linear with the B field. An electron density of $\sim 6.8 \times 10^{11}$ cm^{-2} and mobility of $\sim 1 \times 10^6$ cm^2/(V s) are deduced for this InAs QW. At high B fields, well-documented QHE is observed: R_{xx} is vanishingly small, whereas R_{xy} is quantized to the value of $h/\nu e^2$, where ν is the Landau level filling factor, h the Planck constant, and e the electron charge. The observation of well-developed QHE attests to the high quality of the starting InAs QW. Figure 3b presents the magnetotransport data in a MSL specimen. The lattice constant for triangular lattice is 250 nm, and the twist angle is 5°. At low B fields, R_{xx} and R_{xy} largely resemble those in the nonpatterned sample. A carrier density $\sim 7.4 \times 10^{11}$ cm^{-2} can be deduced. At high B fields, however, transport features in R_{xx} become very different from the nonpatterned counterpart. Particularly, in the $\nu = 5$ quantum Hall state, strong in-gap states are observed. Moreover, the strong in-gap states in our MSL device only appears in the R_{xx} trace, and there is no visible change in R_{xy}. In fact, R_{xy} remains quantized to the expected value of $h/5e^2$. This is anomalous, given that in the quantum Hall regime a dissipative nonzero R_{xx} always accompanies a nonquantized Hall resistance. As we shall analyze below using the Diophantine equation, our system realizes an extreme limit that has never been achieved by graphene and TMD moirés. In Figure 3c, for R_{xx} and R_{xy}, the two traces for the B field sweeping up and down overlap with each other perfectly. This demonstrates the reproducibility of the in-gap states and that they are not artifacts.

Now we use the Diophantine equation, $n/n_s = t\phi/\phi_0 + s$,[36,37] which has been widely used to analyze the magnetotransport data of moiré systems[3,38−41] in order to analyze the strong in-gap states. Here t is the integer (or fractional) value of the quantized Hall conductance, s is the filling of mini energy bands for a periodically modulated 2DEG, $n_s = 1/A$ with A the area of the superlattice unit cell, $\phi = BA$ the magnetic flux, and $\phi_0 = h/e$ the magnetic flux quantum. For the sake of data analysis, we rewrite this equation as $n = tB/\phi_0 + s/A$. Then, it follows that each R_{xx} minimum corresponds to an integer value of s, with the constraint that all of their resulting $(n\phi_0 - tB)/s$ values should yield the same constant ϕ_0/A. Table 1 lists the corresponding magnetic field B and the fitted parameter values of (t, s) for each in-gap R_{xx} minimum. In Figure 3d, we plot the value of $(n\phi_0 - tB)/s$ as a function of B, and all of the data points indeed fall onto a line of a constant value of ∼0.15, from which we deduce $A \sim 28 \times 10^{-15}$ m^2. Remarkably, while this area is much smaller than the area of the MSL unit cell ($\sim 8.1 \times 10^{-12}$ m^2), it is surprisingly close to the area of the triangular AG unit cell shown in Figure 1c.

Table 1. Corresponding Magnetic Field B and the Fitted Parameter Values of (t, s) for Each In-Gap R_{xx} Minimum Based on the Diophantine Equation $(n\phi_0 - t \times B)/s = \phi_0/A$

B field	t	s	$(nh/e - tB)/s$
5.99	5	6	0.145
6.05	5	4	0.147
6.26	5	−3	0.146
6.38	5	−8	0.132
6.62	5	−16	0.140
7.08	4	18	0.139
7.20	4	14	0.146
7.28	4	12	0.144

A couple of remarks are in order. First, in principle, the Diophantine equation should include both the AG and MSL potential modulations as follows: $n = tB/\phi_0 + s_1/A_1 + s_2/A_2$, where A_1 and A_2 are the areas of AG and MSL unit cells,

https://doi.org/10.1021/acs.nanolett.5c02180
Nano Lett. XXXX, XXX, XXX−XXX

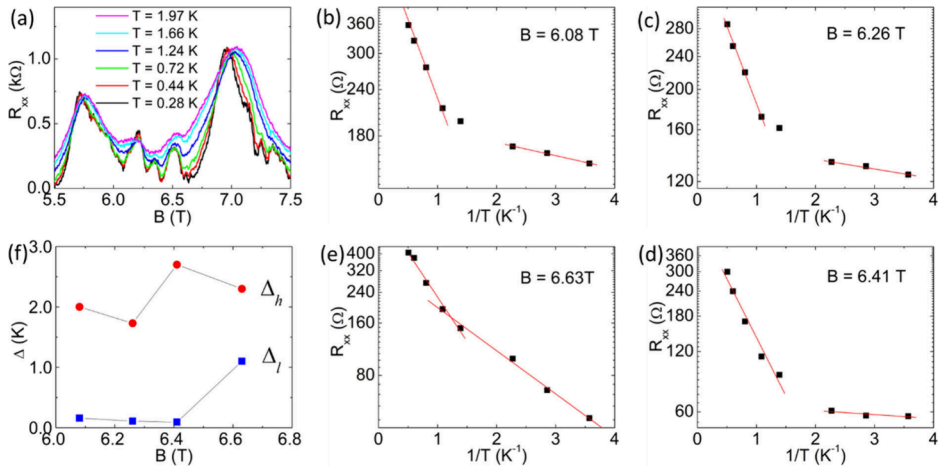

Figure 4. Energy gaps of the anomalous in-gap states. (a) Temperature dependence of R_{xx} for the in-gap states in the $\nu = 5$ quantum Hall state. (b–e) Arrhenius plots for the four in-gap states at the magnetic fields $B = 6.08$, 6.26, 6.41, and 6.63 T, respectively. It is clearly seen that there exist two slopes for each case, signaling a two-gap nature for the in-gap states. (f) Energy gaps plotted as a function of the magnetic field.

respectively. Because $A_2 = 8.1 \times 10^{-12}$ m^2 is much larger than $A_1 = 2.8 \times 10^{-14}$ m^2, for a practical s_2, s_2/A_2 is negligibly small. Thus, the Diophantine equation is dominated by the AG physics. Second, for $t = 5$, $A_2 = 8.1 \times 10^{-12}$ m^2, and a fixed s_1, the change in B needed for a change in s_2 by 1 is ∼0.1 mT. Given the specifics of InAs, $\delta B = 0.1$ mT corresponds to an energy variation of 1 mK (here we take $B = 6.5$ T), much smaller than the sample temperature ∼300 mK in our cryogenic system. Thus, to observe any change in s_2, one needs to reduce A_2 by either increasing the twist angle or to reduce the AG lattice constant from 250 nm to, e.g., 20 nm.

These strong in-gap states must originate from the moiré engineering. Indeed, for comparison, only much weaker R_{xx} minima are observed in the QHE regime of an AG sample made with the same InAs QW (see the Supporting Information and ref 42). Importantly, the same quantum Hall state is observed at multiple miniband fillings at a fixed density but a varying B field. As a previously unexplored regime, this is in sharp contrast to the graphene and TMD moiré systems in which multiple quantum Hall or Chern insulator states are observed at the same miniband filling.[38−41] While the graphene and TMD moirés generally exhibit $B/\phi_0 \ll s/A$, our experimental system realizes the opposite limit, $B/\phi_0 \gg s/A$, for the first time, because of the large supercell area A. As we vary the magnetic field B, the miniband index s swipes through a series of integers, while the Chern number t remains unchanged. Additionally, in our 2DEG-based MSL, the two AGs are defined in the same 2DEG plane and thus strongly coupled. This is also different from vdW moiré systems in which the interlayer couplings are weak.

To further characterize these in-gap states, we carry out temperature-dependent studies of R_{xx} of the strong in-gap states within the same $\nu = 5$ quantum Hall state, as shown in Figure 4a. Clearly, thermally activated behavior is observed for each in-gap state, and the R_{xx} minima increases with temperature. In Figure 4b–e, an Arrhenius plot is displayed for the in-gap states at $B = 6.05$, 6.26, 6.38, and 6.62 T. The red lines are linear fits. It is apparent that, for each in-gap state, there exist two gaps, one for high temperatures (Δ_h) and the other for low temperatures (Δ_l). In Figure 4f, the energy gaps for these in-gap states are plotted as a function of B. As aforementioned, our system is in the previously unexplored limit, $B/\phi_0 \gg s_1/A_1 \gg s_2/A_2$, because of the large AG unit-cell area A_1 and the even larger MSL unit-cell area A_2. Thus, as we vary the magnetic field B, the miniband indexes s_1 and $s_2$swipe through a series of integers, while the Chern number t remains unchanged. For this reason, we assign the larger gap Δ_h to the relatively strong AG gap and the smaller gap Δ_l to the relatively weak MSL gap.

In closing, we note that it was generally believed that the Hofstadter butterfly spectrum can only be observable in the limit of $\phi/\phi_0 \sim 1$.[36] Surprisingly, the results in our MSL specimen show that the butterfly spectrum is still observable when $\phi/\phi_0 \sim 20$. This new limit may have important implications for studying new many-body states emergent in 2DEG-based MSLs. Lastly, semiconductors such as GaAs and InAs have been the "go-to" materials over the past five decades for classical information technology and may continue their primacy in the quantum era. By engineering their heterostructures into an artificial quantum materials platform, future applications can take the advantage of state-of-the-art semiconductor synthesis and processing such as (1) crystalline perfection and purity, (2) advanced fabrication techniques, (3) precise reproducibility of AG and MSL without the notorious twist-angle disorder, and (4) compositional control via epitaxy of III−V materials, including heavy (In and Sb) and light (Ga and As) elements for tuning the strength of SOCs and vertical engineering for tailoring band topology.

METHODS

Electronic Transport Measurements. A specimen of 4 mm × 4 mm is cleaved from a MSL patterned wafer and indium contacts are placed along the edge and corner of the specimen. Low-frequency (∼11 Hz) lock-in amplifier techniques with an excitation current of ∼10 nA is used to measure the transport coefficients R_{xx} and R_{xy}. All data are taken in pumped 3He systems, and devices are immersed in liquid 3He.

Band Structure Calculations. The AG band structures displayed in Figure 2 were calculated using the model of muffin-tin potentials.[19] As shown in Figure 1a, the triangular lattice of white holes acts as a barrier for electrons and thus produces a honeycomb lattice formed by the red dots. For the single layer AG, we set the strength of the potential given by

https://doi.org/10.1021/acs.nanolett.5c02180
Nano Lett. XXXX, XXX, XXX−XXX

the holes to $V = 10\frac{h^2}{2m^*L^2}$ and their radii to $R = \frac{1}{9}L$ and Fourier-transformed the muffin-tin potential to the momentum space. Then the Bloch Hamiltonian was diagonalized over a basis of plane-wave states, with an energy cutoff $E_c = \left(\frac{200}{3}\right)\frac{h^2}{m^*L^2} = \frac{40}{3}V$ to ensure convergence of the low-energy band structure. When necessary, an effective mass of $m^* = 0.023m_e$ (for InAs) and a lattice constant $L = 200$ nm (for IL) were adopted. The commensurate MSL features two identical AG, with the same parameters V and R but rotated at a twist angle θ without any relative translation. For the MSL calculations, the same energy cutoff E_c was used.

■ ASSOCIATED CONTENT

Supporting Information

The Supporting Information is available free of charge at https://pubs.acs.org/doi/10.1021/acs.nanolett.5c02180.

Electronic transport in an AG sample and the Diophantine analysis and tunable strong SOC in AG (PDF)

■ AUTHOR INFORMATION

Corresponding Authors

Wei Pan − *Sandia National Laboratories, Livermore, California 94551, United States;* orcid.org/0000-0002-5629-5296; Email: wpan@sandia.gov

Fan Zhang − *Department of Physics, The University of Texas at Dallas, Richardson, Texas 75080, United States;* Email: zhang@utdallas.edu

Authors

D. Bruce Burckel − *Sandia National Laboratories, Albuquerque, New Mexico 87185, United States*

Catalin D. Spataru − *Sandia National Laboratories, Livermore, California 94551, United States*

Keshab R. Sapkota − *Sandia National Laboratories, Albuquerque, New Mexico 87185, United States;* orcid.org/0000-0001-8581-4211

Aaron J. Muhowski − *Sandia National Laboratories, Albuquerque, New Mexico 87185, United States*

Samuel D. Hawkins − *Sandia National Laboratories, Albuquerque, New Mexico 87185, United States*

John F. Klem − *Sandia National Laboratories, Albuquerque, New Mexico 87185, United States*

Layla S. Smith − *Department of Physics, Norfolk State University, Norfolk, Virginia 23504, United States; Sandia National Laboratories, Livermore, California 94551, United States*

Doyle A. Temple − *Department of Physics, Norfolk State University, Norfolk, Virginia 23504, United States*

Zachery A. Enderson − *Oak Ridge Institute for Science and Education Postdoctoral Fellowship, Oak Ridge, Tennessee 37831, United States; School of Physics, Georgia Institute of Technology, Atlanta, Georgia 30332, United States;* orcid.org/0000-0002-4919-8770

Zhigang Jiang − *School of Physics, Georgia Institute of Technology, Atlanta, Georgia 30332, United States;* orcid.org/0000-0001-9884-3337

Komalavalli Thirunavukkuarasu − *Department of Physics, Florida A&M University, Tallahassee, Florida 32307, United States; National High Magnetic Field Laboratory, Tallahassee, Florida 32310, United States;* orcid.org/0000-0001-6148-2670

Li Xiang − *National High Magnetic Field Laboratory, Tallahassee, Florida 32310, United States*

Mykhaylo Ozerov − *National High Magnetic Field Laboratory, Tallahassee, Florida 32310, United States;* orcid.org/0000-0002-5470-1158

Dmitry Smirnov − *National High Magnetic Field Laboratory, Tallahassee, Florida 32310, United States;* orcid.org/0000-0001-6358-3221

Chang Niu − *School of Electrical and Computer Engineering, Purdue University, West Lafayette, Indiana 47907, United States;* orcid.org/0000-0003-3175-7164

Peide D. Ye − *School of Electrical and Computer Engineering, Purdue University, West Lafayette, Indiana 47907, United States;* orcid.org/0000-0001-8466-9745

Praveen Pai − *Department of Physics, The University of Texas at Dallas, Richardson, Texas 75080, United States*

Complete contact information is available at: https://pubs.acs.org/10.1021/acs.nanolett.5c02180

Author Contributions

W.P., D.B.B., C.D.S., J.F.K., and F.Z. conceived the project. A.J.M., S.D.H., and J.F.K. contributed to the materials design and growth. W.P., D.B.B., K.R.S., and C.N. contributed to the device fabrication. W.P., L.S.S., Z.A.E., K.T., L.X., M.O., and D.S. contributed to the characterization and measurements. C.D.S. and P.P. contributed to theoretical simulations. D.A.T. supervised the work at Norfolk State University, Z.J. supervised the work at Georgia Institute of Technology, P.D.Y. supervised the work at Purdue University, and F.Z. supervised the work at The University of Texas at Dallas. W.P. and F.Z. wrote the manuscript with inputs from all authors.

Notes

The authors declare no competing financial interest.

■ ACKNOWLEDGMENTS

We are grateful to Jeff Tsao at Sandia National Laboratories for his many insightful comments and suggestions during the writing of this manuscript. Work at Sandia National Laboratories was supported by the LDRD program. W.P. and K.T. acknowledge support from the Department of Energy (DOE), under Grant DE-SC0024486. W.P. also acknowledges support from the DOE/BES Microelectronics Science Research Center. Z.J. and K.T. acknowledge support from the Georgia Tech Research Collaboration Forum Seed Grant. Z.J., L.X., and D.S. acknowledge support from the DOE, under Grant DE-FG02-07ER46451. P.P. and F.Z. were supported by the National Science Foundation (NSF) under Grants DMR-1945351, DMR-2324033, and DMR-2414726; they acknowledge the Texas Advanced Computing Center (TACC) for providing resources that have contributed to the research results reported in this work. Part of the measurements were carried out at the National High Magnetic Field Laboratory, which is supported by the NSF Cooperative Agreement (No. DMR-2128556) and the State of Florida. Part of the device fabrication was performed at the Center for Integrated Nanotechnologies, a U.S. DOE, Office of BES, user facility. Sandia National Laboratories is a multimission laboratory managed and operated by National Technology and Engineering Solutions of Sandia LLC, a wholly owned subsidiary of Honeywell International Inc. for the U.S. DOE's National

Nuclear Security Administration under Contract DE-NA0003525. This written work is authored by an employee of NTESS. The employee, not NTESS, owns the right, title and interest in and to the written work and is responsible for its contents. Any subjective views or opinions that might be expressed in the written work do not necessarily represent the views of the U.S. Government. The publisher acknowledges that the U.S. Government retains a nonexclusive, paid-up, irrevocable, worldwide license to publish or reproduce the published form of this written work or allow others to do so, for U.S. Government purposes. The DOE will provide public access to results of federally sponsored research in accordance with the DOE Public Access Plan.

REFERENCES

(1) Tokura, Y.; Kawasaki, M.; Nagaosa, N. Emergent functions of quantum materials. *Nat. Phys.* **2017**, *13*, 1056−1068.
(2) Andrei, E. Y.; Efetov, D. K.; Jarillo-Herrero, P.; MacDonald, A. H.; Mak, K. F.; Senthil, T.; Tutuc, E.; Yazdani, A.; Young, A. F. The marvels of moiré materials. *Nature Reviews Materials* **2021**, *6*, 201.
(3) Lau, C. N.; Bockrath, M. W.; Mak, K. F.; Zhang, F. Reproducibility in the fabrication and physics of moiré materials. *Nature* **2022**, *602*, 41−50.
(4) Kurebayashi, H.; Garcia, J. H.; Khan, S.; Sinova, J.; Roche, S. Magnetism, symmetry and spin transport in van der Waals layered systems. *Nature Reviews Phys.* **2022**, *4*, 150−166.
(5) Törmä, P.; Peotta, S.; Bernevig, B. A. Superconductivity, superfluidity and quantum geometry in twisted multilayer systems. *Nature Reviews Phys.* **2022**, *4*, 528−542.
(6) Mak, K. F.; Shan, J. Semiconductor moire materials. *Nat. Nanotechnol.* **2022**, *17*, 686−695.
(7) Ma, C.; Yuan, S.; Cheung, P.; Watanabe, K.; Taniguchi, T.; Zhang, F.; Xia, F. Intelligent infrared sensing enabled by tunable moiré quantum geometry. *Nature* **2022**, *604*, 266−272.
(8) Hu, X.; Hyart, T.; Pikulin, D. I.; Rossi, E. Geometric and Conventional Contribution to the Superfluid Weight in Twisted Bilayer Graphene. *Phys. Rev. Lett.* **2019**, *123*, No. 237002.
(9) Dean, C. R.; et al. Hofstadter's butterfly and the fractal quantum Hall effect in moiré superlattices. *Nature* **2013**, *497*, 598.
(10) Hunt, B.; et al. Massive Dirac Fermions and Hofstadter Butterfly in a van der Waals Heterostructure. *Science* **2013**, *340*, 1427.
(11) Park, H.; Cai, J.; Anderson, E.; Zhang, Y.; Zhu, J.; Liu, X.; Wang, C.; Holtzmann, W.; Hu, C.; Liu, Z.; Taniguchi, T.; Watanabe, K.; Chu, J.-H.; Cao, T.; Fu, L.; Yao, W.; Chang, C.Z.; Cobden, D.; Xiao, D.; Xu, X. Observation of fractionally quantized anomalous Hall effect. *Nature* **2023**, *622*, 74−79.
(12) Lu, Z.; Han, T.; Yao, Y.; Reddy, A. P.; Yang, J.; Seo, J.; Watanabe, K.; Taniguchi, T.; Fu, L.; Ju, L. Fractional quantum anomalous Hall effect in multilayer graphene. *Nature* **2024**, *626*, 759−764.
(13) Kang, K.; Shen, B.; Qiu, Y.; Zeng, Y.; Xia, Z.; Watanabe, K.; Taniguchi, T.; Shan, J.; Mak, K. F. Evidence of the fractional quantum spin Hall effect in moiré MoTe2. *Nature* **2024**, *628*, 522−526.
(14) Suárez Morell, E.; Correa, J. D.; Vargas, P.; Pacheco, M.; Barticevic, Z. Flat bands in slightly twisted bilayer graphene: Tight-binding calculations. *Phys. Rev. B* **2010**, *82*, No. 121407.
(15) Bistritzer, R.; MacDonald, A. H. Moiré bands in twisted double-layer graphene. *Proc. Natl. Acad. Sci. U.S.A.* **2011**, *108*, 12233.
(16) Cao, Y.; Fatemi, V.; Fang, S.; Watanabe, K.; Taniguchi, T.; Kaxiras, E.; Jarillo-Herrero, P. Unconventional superconductivity in magic-angle graphene superlattices. *Nature* **2018**, *556*, 43.
(17) Yankowitz, M.; Chen, S.; Polshyn, H.; Zhang, Y.; Watanabe, K.; Taniguchi, T.; Graf, D.; Young, A. F.; Dean, C. R. Tuning superconductivity in twisted bilayer graphene. *Science* **2019**, *363*, 1059.
(18) Tian, H.; Gao, X.; Zhang, Y.; Che, S.; Xu, T.; Cheung, P.; Watanabe, K.; Taniguchi, T.; Randeria, M.; Zhang, F.; Lau, C. N.; Bockrath, M. W. Evidence for Dirac flat band superconductivity enabled by quantum geometry. *Nature* **2023**, *614*, 440−444.
(19) Sharpe, A. L.; Fox, E. J.; Barnard, A. W.; Finney, J.; Watanabe, K.; Taniguchi, T.; Kastner, M. A.; Goldhaber-Gordon, D. Emergent ferromagnetism near three-quarters filling in twisted bilayer graphene. *Science* **2019**, *365*, 605.
(20) Tschirhart, C. L.; Serlin, M.; Polshyn, H.; Shragai, A.; Xia, Z.; Zhu, J.; Zhang, Y.; Watanabe, K.; Taniguchi, T.; Huber, M. E.; Young, A. F. Imaging orbital ferromagnetism in a moiré Chern insulator. *Science* **2021**, *372*, 1323−1327.
(21) Uri, A.; Grover, S.; Cao, Y.; Crosse, J. A.; Bagani, K.; Rodan-Legrain, D.; Myasoedov, Y.; Watanabe, K.; Taniguchi, T.; Moon, P.; Koshino, M.; Jarillo-Herrero, P.; Zeldov, E. Mapping the twist-angle disorder and Landau levels in magic-angle graphene. *Nature* **2020**, *581*, 47−52.
(22) Ghorashi, S. A. A.; Dunbrack, A.; Abouelkomsan, A.; Sun, J.; Du, X.; Cano, J. Topological and Stacked Flat Bands in Bilayer Graphene with a Superlattice Potential. *Phys. Rev. Lett.* **2023**, *130*, No. 196201.
(23) Park, C. H.; Louie, S. G. Making Massless Dirac Fermions from a Patterned Two-Dimensional Electron Gas. *Nano Lett.* **2009**, *9*, 1793.
(24) Du, L.; Liu, Z.; Wind, S. J.; Pellegrini, V.; West, K. W.; Fallahi, S.; Pfeiffer, L. N.; Manfra, M. J.; Pinczuk, A. Observation of Flat Bands in Gated Semiconductor Artificial Graphene. *Phys. Rev. Lett.* **2021**, *126*, No. 106402.
(25) Wang, D. Q.; Krix, Z.; Sushkov, O. P.; Farrer, I.; Ritchie, D. A.; Hamilton, A. R.; Klochan, O. Formation of Artificial Fermi Surfaces with a Triangular Superlattice on a Conventional Two-Dimensional Electron Gas. *Nano Lett.* **2023**, *23*, 1705−1710.
(26) Miller, J. B.; Zumbühl, D. M.; Marcus, C. M.; Lyanda-Geller, Y. B.; Goldhaber-Gordon, D.; Campman, K.; Gossard, A. C. Gate-Controlled Spin-Orbit Quantum Interference Effects in Lateral Transport. *Phys. Rev. Lett.* **2003**, *90*, No. 076807.
(27) Arora, H. S.; et al. Superconductivity in metallic twisted bilayer graphene stabilized by WSe2. *Nature* **2020**, *583*, 379.
(28) Lin, J.-X.; Zhang, Y.-H.; Morissette, E.; Wang, Z.; Liu, S.; Rhodes, D.; Watanabe, K.; Taniguchi, T.; Hone, J.; Li, J. I. A. Spin-orbit−driven ferromagnetism at half moiré filling in magic-angle twisted bilayer graphene. *Science* **2022**, *375*, 437−441.
(29) Yu, W.; et al. Anomalously large resistance at the charge neutrality point in a zero-gap InAs/GaSb bilayer. *New J. Phys.* **2018**, *20*, No. 053062.
(30) Lyo, S. K.; Pan, W. Excitons in coupled type-II double quantum wells under electric and magnetic fields: InAs/AlSb/GaSb. *J. Appl. Phys.* **2015**, *118*, No. 195705.
(31) Liu, C.; Hughes, T. L.; Qi, X. L.; Wang, K.; Zhang, S. C. Quantum spin Hall effect in inverted type-II semiconductors. *Physical review letters* **2008**, *100*, No. 236601.
(32) Naveh, Y.; Laikhtman, B. Excitonic instability and electric-field-induced phase transition towards a two-dimensional exciton condensate. *Phys. Rev. Lett.* **1996**, *77*, 900.
(33) Pikulin, D. I.; Hyart, T. Interplay of exciton condensation and the quantum spin Hall effect in InAs/GaSb bilayers. *Phys. Rev. Lett.* **2014**, *112*, No. 176403.
(34) Ruiz, D. B.; Sheinfux, H. H.; Hoffmann, R.; Torre, I.; Agarwal, H.; Kumar, R. K.; Vistoli, L.; Taniguchi, T.; Watanabe, K.; Bachtold, A.; Koppens, F. H. L. Engineering high quality graphene superlattices via ion milled ultra-thin etching masks. *Nat. Commun.* **2022**, *13*, 6926.
(35) Wang, S.; Scarabelli, D.; Du, L.; Kuznetsova, Y. Y.; Pfeiffer, L. N.; West, K. W.; Gardner, G. C.; Manfra, M. J.; Pellegrini, V.; Wind, S. J.; Pinczuk, A. Observation of Dirac bands in artificial graphene in small-period nanopatterned GaAs quantum wells. *Nat. Nanotechnol.* **2018**, *13*, 29.
(36) Streda, P. Quantised Hall effect in a two-dimensional periodic potential. *J. Phys. C* **1982**, *15*, 1299−1303.
(37) Albrecht, C.; Smet, J. H.; von Klitzing, K.; Weiss, D.; Umansky, V.; Schweizer, H. Evidence of Hofstadter's Fractal Energy Spectrum in the Quantized Hall Conductance. *Phys. Rev. Lett.* **2001**, *86*, 147.

https://doi.org/10.1021/acs.nanolett.5c02180
Nano Lett. XXXX, XXX, XXX−XXX

(38) Nuckolls, K. P.; Oh, M.; Wong, D.; Lian, B.; Watanabe, K.; Taniguchi, T.; Bernevig, B. A.; Yazdani, A. Strongly correlated Chern insulators in magic-angle twisted bilayer graphene. *Nature* **2020**, *588*, 610−615.
(39) Saito, Y.; Ge, J.; Rademaker, L.; Watanabe, K.; Taniguchi, T.; Abanin, D. A.; Young, A. F. Hofstadter subband ferromagnetism and symmetry-broken Chern insulators in twisted bilayer graphene. *Nat. Phys.* **2021**, *17*, 478−481.
(40) Xie, Y.; Pierce, A. T.; Park, J. M.; Parker, D. E.; Khalaf, E.; Ledwith, P.; Cao, Y.; Lee, S. H.; Chen, S.; Forrester, P. R.; Watanabe, K.; Taniguchi, T.; Vishwanath, A.; Jarillo-Herrero, P.; Yacoby, A. Fractional Chern insulators in magic-angle twisted bilayer graphene. *Nature* **2021**, *600*, 439−443.
(41) Wu, S.; Zhang, Z.; Watanabe, K.; Taniguchi, T.; Andrei, E. Y. Chern insulators, van Hove singularities and topological flat bands in magic-angle twisted bilayer graphene. *Nat. Mater.* **2021**, *20*, 488−494.
(42) Spataru, C. D.; Pan, W.; Cerjan, A. Topological phenomena in artificial quantum materials revealed by local Chern markers. *Phys. Rev. Lett.* **2025**, *134*, No. 126601.

https://doi.org/10.1021/acs.nanolett.5c02180
Nano Lett. XXXX, XXX, XXX−XXX